Icephobicity and durability assessment of superhydrophobic surfaces: the role of surface roughness and the ice adhesion measurement technique

K. Maghsoudi, E. Vazirinasab, G. Momen, R. Jafari*

Department of Applied Sciences, University of Quebec in Chicoutimi (UQAC)

555, boul. de l'Université, Chicoutimi, Québec, G7H 2B1, Canada

** E-mail: Khosrow.maghsoudi1@uqac.ca*

Abstract

The durability of anti-wetting properties is of great importance for ensuring long-lasting superhydrophobic and icephobic surfaces that require minimal maintenance and resurfacing. Herein, we fabricated superhydrophobic silicone rubber surfaces having ultra-water repellency and icephobic properties via two industrially applicable methods: micro compression molding (μCM) and atmospheric pressure plasma (APP) treatment. We produced surfaces covered by micro-nanostructures of differing sizes. We evaluated the anti-icing properties (delayed ice formation) and de-icing properties (reduced ice adhesion strength) of the produced surfaces that were subjected to two forms of icing conditions. The well-known ice adhesion measurement techniques, i.e., the centrifuge adhesion and push-off tests, provided quantitative comparisons of the ice adhesion strength of the produced surfaces. We observed two different mechanical deformations during the ice detachment from the surfaces. Although both superhydrophobic surfaces reduced ice adhesion strength, the smaller surface micro-nanostructures produced a greater reduction in ice adhesion by favoring less ice interlocking with the surface asperities. To rigorously assess the durability of the produced surfaces, we carried out a comprehensive series of experiments that covered a wide range of real-life conditions. Under harsh environmental conditions, the surfaces maintained a water contact angle and contact angle hysteresis of >150° and <10°, respectively, thereby confirming the resistance of the superhydrophobic silicone surfaces to severe chemical and mechanical damage. In some cases where water repellency was lost, the silicone rubber surfaces demonstrated a satisfactory recovery of their anti-wetting properties.

Keywords: Superhydrophobicity; Icephobicity; Anti-icing; Ice adhesion measurement; Durability; Recovery.

1. Introduction

Water-repellent superhydrophobic surfaces are determined by a water contact angle (WCA) >150° and a contact angle hysteresis (CAH) or sliding angle (SA) <10°. Maghsoudi et al. (2019) declared that for a material to demonstrate superhydrophobic properties, it usually fulfills two prerequisites: 1) having the non-polar groups on the surface as the hydrophobic characteristics and 2) the presence of micro-nanofeatures that roughen the surface. Among multiple approaches for fabrication of superhydrophobic surfaces, Maghsoudi et al. (2020) reviewed that direct replication method including micro injection molding, micro compression molding, and hot embossing is advantageous for mass production. In addition, Vazirinasab et al. (2019) demonstrated that surface treatment by atmospheric pressure plasma is an industrially conceivable facile approach. Superhydrophobic surfaces have been the focus of multiple recent studies due to their wide range of applications. Vazirinasab et al. (2018) expressed that these applications include anti-wetting, anti-icing, low-adhesion, low-drag, corrosion resistant, buoyancy enhancement, and self-cleaning applications. Recently, potential applications of superhydrophobic surfaces have been studied by many researchers. Huang et al. (2020) developed superhydrophobic filtrating materials for application to oil/water separation. Yuan et al. (2018) showed how hierarchical superhydrophobic structures exhibited excellent adsorption capacity for fast and selective oil/water separation. Li et al. (2020) studied the droplet dynamics on well-defined structured superhydrophobic surfaces which is highly important in self-transportation of droplets.

Superhydrophobic surfaces are among the best candidate surfaces for exhibiting icephobic properties. Alizadeh et al. (2012) showed that such water-repelling surfaces can delay ice formation, known as the anti-icing property, and Momen et al. (2014) observed reduced ice adhesion strength for superhydrophobic surfaces, known as the de-icing property. Ice formation on a superhydrophobic surface having micro-nanostructures is affected by (1) the reduced area in contact between the substrate and water droplets due to the high WCA. Yancheshme et al. (2020) stated that this scenario leads to a reduced heat transfer via conduction, (2) Shen et al. (2015) found that the trapped air between the surface micro-nanostructures acting as an insulating layer reduces the heat transfer, (3) Eberle et al. (2014) considered the limited number of sites at the solid-liquid interface available for the heterogeneous nucleation of ice, and (4) Yao et al. (2017) took the shorter rebounding time—shorter rest time—of water droplets compared to the nucleation time into account. Moreover, Ling et al. (2016) showed that the reduced ice adhesion strength was due to the formation of microcracks caused by surface roughness causing interfacial stress concentrations, and the reduced contact area between the formed ice and the surface due to the limited solid–liquid contact area. However, Ling et al. (2016) also stated that surface roughness may negatively affect icephobicity due to the interlocked ice within the surface structures. This mechanical interlocking is governed by the stability

of the Cassie-Baxter regime. Although there is, on one hand, a fully Cassie-Baxter state and, on the other, a Wenzel state, Cansoy et al. (2011) showed that an intermediate state can exist where a water droplet penetrates partially into the surface structures. Li et al. (2018) declared that the degree of this penetration can affect the mechanical interlocking of ice producing either a "Cassie ice" or "Wenzel ice". Consequently, the surface geometry has a decisive effect on the icephobic behavior of the produced surfaces. Among the various surface geometries, including microstructures, nanostructures, and hierarchical micro-nanostructures, He et al. (2014) determined that hierarchical micro-nanostructures have demonstrated the lowest ice adhesion strength. Moreover, the effect of ice type on the icephobic properties of a certain surface is worth studying. According to Ryerson (2011), atmospheric icing phenomena are divided into glaze ice, hard rime, and frost having a density of 0.7-0.9, 0.3-0.7, and <0.1 g/cm^3, respectively. Rime ice and frost are formed from the fogs and in-clouds containing supercooled droplets, while glaze ice can be produced by both the precipitation (freezing rain or drizzle) and in-cloud icing. Stenroos (2015) reported that the droplet sizes vary between few μm to 50 μm for the in-cloud icing and from 100 μm to several mm for the precipitation icing. Fortin et al. (2012, Liu et al. (2012) reported that the greatest ice adhesion strength belongs to glaze ice. Work et al. (2018) reviewed that in many studies, the ice adhesion strength of a surface is evaluated against bulk ice rather than atmospheric icing. Consequently, to rigorously assess the icephobic properties of a micro-nanostructured surface, the influence of various ice types should be studied. The ice adhesion measurement technique should also be added to this list. These techniques include centrifugal adhesion test (CAT), shear strength tests (e.g. push-off and zero-degree cone tests), and tensile strength test. For a certain surface, the ice adhesion results obtained from the different techniques are not necessarily identical. Rønneberg et al. (2020) claimed that this difference can stem from either the nature and conditions of the employed adhesion test or the behavior of the ice-solid interface subjected to the ice detachment.

Although multiple applications benefit from superhydrophobic surfaces, the durability of these surfaces against mechanical forces and chemical media remains questionable. Golovin et al. (2017) described that in general, superhydrophobic surfaces prone to mechanical or chemical damage either lose surface roughness or the low surface energy chemical bonds. This fragility can lead to a transition from the Cassie-Baxter state to the Wenzel state, a state that is energetically more favorable for the water droplet. Milionis et al. (2016) showed that the transition to the Wenzel state induces a strong pinning that increases the adhesion between the water droplet and the substrate; the result is a loss of water repellency or anti-wetting performance of the surface. The lack of a defined standard procedure for evaluating the durability of different types of superhydrophobic surfaces has led to a myriad of set-ups and procedures to measure surface durability. These durability measurements are divided into tests of mechanical durability and chemical resistivity. Mechanical durability analyses include abrasion resistance under a specific force, wear

resistance by rubbing the surface, the tape-peel tests, scratch tests, and fatigue testing. The chemical durability analyses include immersion in aqueous solutions of varying pH, and exposure to UV light, as investigated. Some analyses, such as water droplet impacts and the ultrasonic treatment of surfaces in water involve both mechanical and chemical testing. Therefore, a comprehensive set of tests is required to assess the durability properties of a superhydrophobic and icephobic surface.

Although many investigations have reported changes to ice adhesion strength when surfaces are subjected to various mechanical tests as reviewed by Work et al. (2018), only few studies such as the investigation by Ghalmi et al. (2015), Momen et al. (2015), Jafari et al. (2016), and Mobarakeh et al. (2018) have reported changes of the WCA and CAH after several cycles of icing/de-icing. Of the published results, the WCA generally decreases and the CAH increases after multiple cycles. The adhesive strength and the mechanical bonding between the fabricated micro-nanostructures and the substrate are critical in explaining the wettability of the surfaces following the icing/de-icing cycles. Lazauskas et al. (2013) demonstrated that these cycles can transform a spiky surface morphology into a bumpy surface when the nanostructured protrusions become damaged.

Silicone rubber material has exhibited hydrophobic-recovery properties where low molecular weight silicone (LMWS) chains diffused from the bulk material to the surface. Yan et al. (2015) showed that this self-healing has also been occurred via the reorientation of methyl groups from the bulk material to the surface and the reorientation of hydroxyl groups from the surface into the bulk material by the partial segmental movement of silicone rubber chains. Hillborg et al. (2001) also considered the condensation of silanol groups for such behavior. While Maghsoudi et al. (2019) observed that the migration of LMWS to the surface dominates the hydrophobic recovery of polluted silicone rubber surfaces, Liu et al. (2006) considered the conformational reorientation of groups as the main responsible for the hydrophobic recovery of surfaces when silicone rubber chains become aged or oxidized. Thus, the ability of a surface to recover its anti-wetting properties is as important as the evaluation of the durability of superhydrophobic surfaces.

In the present study, we produce superhydrophobic silicone rubber surfaces using two industrially applicable approaches, i.e., micro compression molding (μCM) and atmospheric pressure plasma (APP) treatment. The produced surfaces showed having a high WCA and very low CAH. The low CAH of both produced surfaces was created by micro-nanostructures that established a Cassie-Baxter regime. Owing to this low CAH, these produced surfaces demonstrated icephobic properties. We assessed the anti-icing and de-icing properties by measuring freezing delay times and ice adhesion strength, respectively. We applied two common methods to measure ice adhesion strength, the centrifuge adhesion (CAT) and push-off tests under various icing conditions. This is, to our knowledge, the first study to investigate the ice adhesion

strength by two methods and two icing conditions to provide a comprehensive comparison. In addition to applying repetitive icing/de-icing cycles to study the durability of the produced surfaces, we also studied the durability of the surfaces under mechanical and chemical forces. We also rigorously examined the recovery of surface hydrophobicity/superhydrophobicity of the silicone surfaces in cases where the superhydrophobicity of a surface was lost.

2. Materials and methods

2.1. Fabrication procedure

We fabricated the superhydrophobic surfaces using high-temperature vulcanized (HTV) silicone rubber materials via a direct replication method (using a micro compression molding, Carver Inc., USA) and an atmospheric pressure plasma machine (Plasmatreat GmbH, Germany) (Fig. 1). The micro-nanostructures on aluminum templates (A6061 alloy) were created by a chemical-etching method—15 wt.% hydrochloric acid solution for 2 h. The curing time of 4.7 min, mold temperature of 149 °C, and molding pressure of 49.7 MPa were selected as compression molding conditions. The selected optimal plasma parameters were a reference voltage of 100%, plasma jet speed of 4 $m \cdot min^{-1}$, gas flow rate of 2500 $L \cdot h^{-1}$, plasma frequency of 21 kHz, a cycle time of 100%, as well as a distance between nuzzle and substrate of 8 mm. The plasma jet passed along the surface four times. (The fabrication procedure is explained in detail in the Supplementary Information).

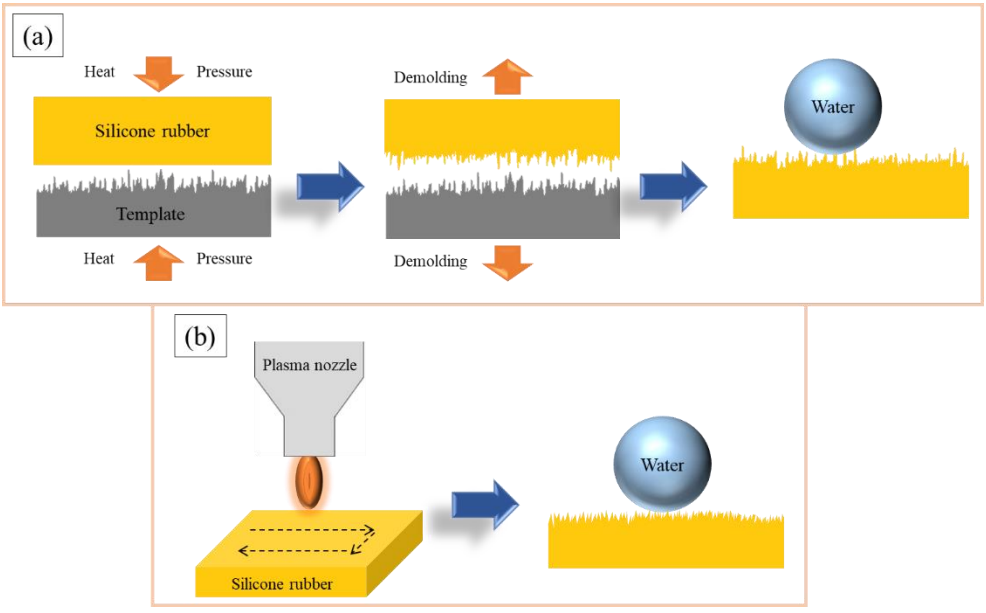

Fig. 1. Schematic of the (a) micro compression molding (μCM) and (b) atmospheric pressure plasma (APP) techniques to create a micro-nanostructured silicone rubber surface.

2.2. Surface characterization

We measured the WCA and CAH using a Kruss™ DSA100 goniometer at 25 ± 0.5 °C. We placed a 4-µL water droplet on the surface and moved it by a needle tip. The difference between the advancing and receding contact angles were reported as CAH. Every reported value equaled the average of measurements at five points on each surface. We relied on scanning electron microscopy (SEM) (JSM-6480 LV SEM manufactured by JEOL Japan) to observe the produced surfaces. The line and area surface roughness were measured using a confocal laser scanning microscope (Profil3D Filmetrics, USA). The surface chemical compositions were determined by Fourier transform infrared spectroscopy (FTIR) using a Cary 630 FTIR Spectrometer (Agilent, USA). The high-quality spectra in the range of 400–4000 cm^{-1} (infrared range) were acquired in ATR (attenuated total reflection) mode. A 4-µL water droplet was observed during the evaporation process, and the digital camera of the Kruss goniometer machine captured the images. The camera images were set at 8× magnification. The software (DSA1 v 1.9, Drop Shape Analysis for DSA100) calculated the contact line length and the contact area with the substrate as a function of time. We therefore monitored changes in the contact line length between the droplet and the surfaces. The temperature of all experiments was identical to that used during the WCA tests.

2.3. Icephobic properties

The WCA of surfaces at below-zero temperatures as well as the freezing delay times were determined in the cold chamber of the Kruss machine. The Peltier cooling stage can reach -30 °C with a control precision of 0.1 °C. The delay in the initiation of water droplet freezing was reported as the freezing delay time. The humidity variation is limited in the closed chamber of the Kruss machine. Moreover, to avoid the influence of condensation on the measurements we used anhydrous calcium sulfate desiccants (Indicating DRIERITE impregnated with cobalt chloride). We determined the ice adhesion strength of the produced samples via two separate methods to obtain a comprehensive comparison of the icephobic properties under various conditions.

For the centrifuge test, samples were iced under freezing drizzle conditions in a climatic chamber at -8.0 ± 0.2 °C by spraying supercooled water microdroplets onto the surfaces. Such conditions resulted in the deposition of glaze ice from the water droplets, having a median volumetric diameter (MVD) of 324 µm on an 1100 ± 70 mm^2 surface and a thickness of around 7 ± 1 mm. Droplet speed corresponded to their free-fall values in the vertical airflow. The samples were iced for about 35 minutes to obtain around 5.5 ± 0.5 g of ice. All samples were iced simultaneously. The samples were tested individually in a centrifuge at -10.0 ± 0.2 °C in a climatic chamber. The centrifugal force (F) was calculated as $F = mr\omega^2$, using the detached ice mass (m), the speed at which the detachment occurred (ω), and the beam radius (r). The ice

adhesion shear stress was calculated as $\tau = F/A$, where A is the iced area. The reduction in ice adhesion was defined as [τ (pristine silicone rubber) - τ (superhydrophobic silicone rubber)]/ τ (pristine silicone rubber).

In the push-off test, a thin 1-cm diameter cylindrical plastic mold was placed onto the substrate. We then filled the mold with deionized water and placed the mold and substrate into a cold chamber at -10.0 ± 0.2 °C for 24 h to make an ice cylinder. Then, we fixed the test sample onto the holder that was gradually pushed toward the force gage at a speed of 0.05 $mm \cdot s^{-1}$. After ice detachment, we calculated the adhesion stress according to the maximum force at the detachment point and the iced area. We calculated the corresponding de-icing energy for each surface using the area under the developed force-displacement curves.

2.4. Durability properties

We used an Elcometer 3000 Clemen Unit (Elcometer, USA) with 4000-grit silicon carbide sandpaper to test the durability of the superhydrophobic surfaces against abrasion. The reason we chose a high grit sandpaper was that a lower sandpaper grit (280–400#) can create superhydrophobicity due to the creation of new surface roughness (added by the sandpaper), while the higher grit, having a relatively smoother surface, deteriorated the superhydrophobic properties by removeing the surface asperities. The applied pressures on the samples' surfaces during abrasion were 1.6 kPa, 3.2 kPa, and 6.4 kPa. We ran the process repeatedly over 2.5 cm of the surface. We measured the WCA and CAH after each block of 50 abrasion cycles.

We also evaluated the durability of the produced silicone rubber surfaces via a finger-press test where a vertical pressure of 80 ± 8.8 kPa was applied to the surface by a bare thumb. We measured the average force applied by a bare thumb using a digital force gauge. To reduce the measurement error, we did these measurements while the hand was stationary. We also carried out a tape-peeling test by applying and removing a pressure-sensitive Scotch-600 tape at approximately 30 kPa pressure to the surface. To test surface durability when subjected to ultrasonication, the surfaces were placed into 100 mL of deionized water in a Branson 2510 ultrasonication bath. After each 60-min interval, we removed the sample, dried the sample for 15 min at 70 °C, then measured the CA. In the continuous water droplet impact durability test, water droplets produced at a rate of 1 $mL \cdot min^{-1}$ from a distance of ~10 cm above the surface fell onto the surface that was placed at a slope of ~5°. The impact point was marked for WCA measurements. Each cycle required 1000 s, during which time ~17 mL water dropped onto the surface. The test ran for 7000 s, i.e., ~120 mL of water in total.

We used buffer solutions having a pH of 2 and 12 as the acidic and alkaline media and used also deionized water (pH 7) to study the durability of the produced surfaces over 15 days. After a 3-day interval, we removed each sample from the solution, rinsed the sample ultrasonically for 15 min, dried the sample at 70 °C for 15 min, and we then measured the WCA and CAH. We used a QUV accelerated weathering tester for the accelerated UV-weathering test to assess the destruction of the surface anti-wetting properties when subjected to simulated outdoor conditions within a controlled laboratory setting. The tests were conducted according to ASTM G154 using UVA-340 fluorescent lamps and a test cycle of 8 h, a temperature of 60 °C, and an irradiance of 0.89 $W \cdot m^{-2}$.

Given the extensive use of HTV silicone rubber in high-voltage insulators, it is relevant to assess the durability of our produced surfaces against harsh weather conditions, e.g., sandstorms. We sandblasted our samples in a sandblasting cabinet under conditions of air blow pressure at 20 psi, an air blower velocity of 10 m/s, a sand feed of 0.07 g/s—thus 4.2 g of sand blown onto the surface after 1 min of air blowing. This amount corresponds to a single sandstorm in Borg-El-Arab, Egypt. Given that Sansom et al. (2015) reported approximately 20 sandstorms per year at this location, a 20-min test simulates one year of exposure to sandstorm conditions. The gun was placed at 25 cm from the sample surface, and the impact angle was set at 90°. We used silicon carbide (SiC) particles to conduct the tests. During a sandstorm, the height to which sands and dust can reach depends on wind strength and the amplitude of wind velocity fluctuations. This height thus varies from 1 m above the ground to 15.24 m. However under similar conditions, Qiang et al. (2007) measured that dust or finer sediments (<63 µm) are lifted higher than coarse sand (>63 µm). On the other hand, a typical height of an electrical transmission tower is 15–50 m; we therefore used a particle size of 18 µm for the test.

3. Results and discussion

3.1. Surface characterization

The WCA and CAH of the pristine silicone rubber surface were 115° ± 1.8° and 43.4° ± 1.9°, respectively. A WCA of 166.6° ± 1.9° and 165.8° ± 1.3° and CAH of 0.6° ± 0.3° and 1.1° ± 0.6° for the µCM and APP-treated silicone rubber surfaces, respectively, testified to the superhydrophobic property of the produced samples. The existence of micro-nanostructures on the silicone surfaces satisfied the required condition of "low surface energy material and surface roughness" to achieve superhydrophobicity. The surface profiles and SEM images of the surfaces at various magnifications are showed in Fig. 2. Surface morphologies differed for each surface. In

Table 1, the line roughness (1D) and area roughness (2D) were provided for comparative purposes (

Table 1). The skewness coefficient (S_{sk}), representing the symmetry level of the surface height relative to the mean plane, and the kurtosis coefficient (S_{ku}), which describes the sharpness of the probability density of the profile, are also provided. In relative to the pristine silicone rubber, the micro compression molding process significantly increased surface roughness. The root-mean-square height (S_q) of the µCM surface increased ~5 times. Although the APP-treated surface possessed almost the same S_q as the pristine surface, the skewness and kurtosis values showed jagged surface structures with considerably higher peaks and lower valleys than those on the pristine surface. This observation was similar to that Vazirinasab et al. (2020) observed in case of a plasma treated Teflon surface compared to a non-treated Teflon surface.

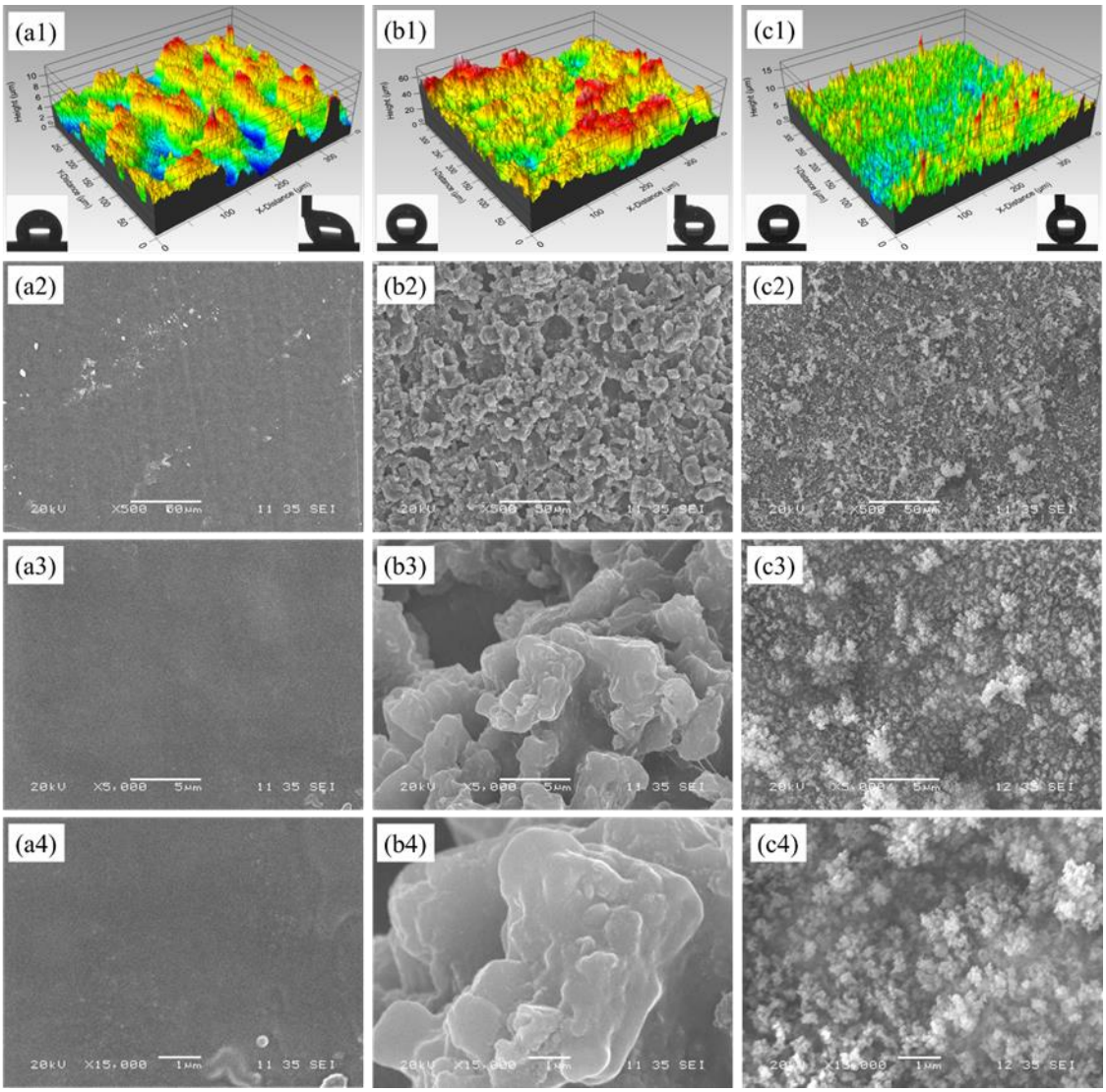

Fig. 2. The 3D surface profiles of the (a1) pristine, (b1) µCM, and (c1) APP-treated silicone rubber surfaces. SEM images of the (a2-a4) pristine, (b2-b4) µCM, and (c2-c4) APP-treated silicone rubber surfaces. Inset images show the WCA and CAH of the corresponding surfaces.

Table 1. Area (2D) and line (1D) roughness values of the µCM and APP-treated silicone rubber surfaces.

	Pristine	µCM	APP
Area roughness (µm)			
Maximum peak to valley height (S_t)	11.68	71.54	16.38
Arithmetic mean height (S_a)	1.46	7.43	1.19
Root mean square height (S_q)	1.76	9.40	1.53
Skewness (S_{sk})	0.07	0.09	0.33
Kurtosis (S_{ku})	2.38	3.008	3.99
Line roughness (µm)			
Maximum peak to valley height (R_t)	5.196	15.16	5.79
Arithmetic mean deviation (R_a)	0.70	2.54	0.70
Root mean square deviation (R_q)	0.89	3.17	0.91

FTIR analysis assessed the contribution of chemical bonds on the fabricated silicone rubber surfaces (Fig. 3). The pristine and µCM surfaces showed identical absorption spectra of Si–$(CH_3)_2$, Si–O–Si, Si(CH_3), and –OH at the positions of 805–855 cm^{-1}, 1000–1110 cm^{-1}, 1245–1275 cm^{-1}, and 3200–3550 cm^{-1}, respectively. For the APP-treated surface, the Si-containing bonds, in particular for Si–$(CH_3)_2$, were modified. Zhang et al. (2012) showed that under plasma treatment, the Si–CH_3 bonds are prone to breakage due to their relatively low binding energy. Moreover, the hydroxyl group (–OH) spectrum almost vanished. Vazirinasab et al. (2019) attributed the disappearance of –OH to the endothermic decomposition of alumina trihydrate (ATH) particles at high temperatures amid the plasma treatment.

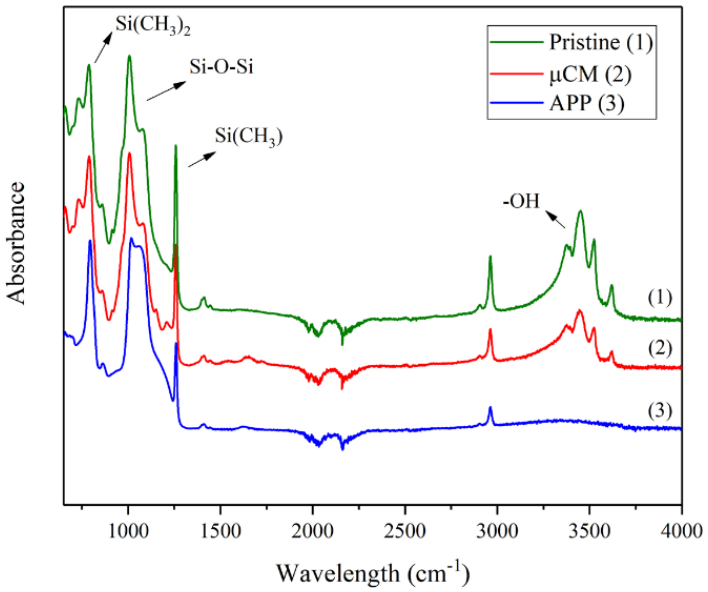

Fig. 3. FTIR spectra for (1) pristine, (2) µCM, and (3) APP-treated silicone rubber surfaces.

The CAH of the fabricated silicone rubber surfaces demonstrated that the dominant wetting regime was Cassie-Baxter due to the created appropriate roughness. However, we then carried out the droplet evaporation test to obtain more understanding about the kinetics of the interfacial interactions. Evaporation occurs when the water molecules diffuse into the environment by convection forces. Three modes of evaporation explain the changes in the WCA and contact line (CL) of a water droplet on a solid surface in calm air. Depending on the WCA or CL being constant or decreased, Khedir et al. (2011) considered the constant contact line (CCL), the constant contact angle (CCA), and the mixed mode. They claimed that the emergence of each mode depends highly on surface geometry and chemistry, which directly influences the wetting regimes.

Fig. 4 presents the evolution of WCA and CL due to the evaporation of small water droplets placed on hydrophobic and superhydrophobic surfaces. On the superhydrophobic surfaces, the water droplets underwent a linear decrease in CL and a gradual reduction of WCA. These observations showed the mobility of the CL due to the low CAH of the superhydrophobic surfaces. Chu et al. (2014) claimed that over time, the water droplet preserved its initial marble-like shape by which a consistent Cassie-Baxter regime could be confirmed. On the pristine surface, however, the steep slope of WCA reduction, with the increase in CL during the first stages of evaporation, and followed by a sharp drop at later stages, indicated the high adhesion of the water droplet to the solid surface. The greater adhesion of the droplet to the pristine surface relative to its adhesion to the superhydrophobic surfaces caused greater evaporation from the upper portion of the droplet on the pristine surface rather than along the triple liquid/solid/air line. This flattens the droplet on the surface, thereby leading to a decreased WCA for the pristine surface. Moreover, the

pinned CL of the pristine surface over the mobile behavior of the CL on the superhydrophobic surfaces led to a different water droplet duration. Dash et al. (2013) described that the longer duration of a water droplet on a superhydrophobic surface, relative to that on a pristine surface, resulted from the high aspect ratio of the droplet, which led to a longer thermal resistance path, and the subsequent low thermal conductivity of the surface due to the trapped air cushions. Moreover, three possibilities exist for water droplet to evaporate on a superhydrophobic surface. Evaporation can occur from the upper portion of the droplet, from the triple line, and from the contact line. The latter causes the presence of a water gas phase within the asperities of the superhydrophobic surfaces. Comparing the behavior of the water droplet on the μCM and APP-treated superhydrophobic surfaces over time revealed that the presence of larger structures on the μCM surface facilitated a greater contact between the water liquid phase and water gas phase trapped within the surface structures. Consequently, the WCA of the μCM surface experienced a greater reduction than that of the APP-treated surface over time.

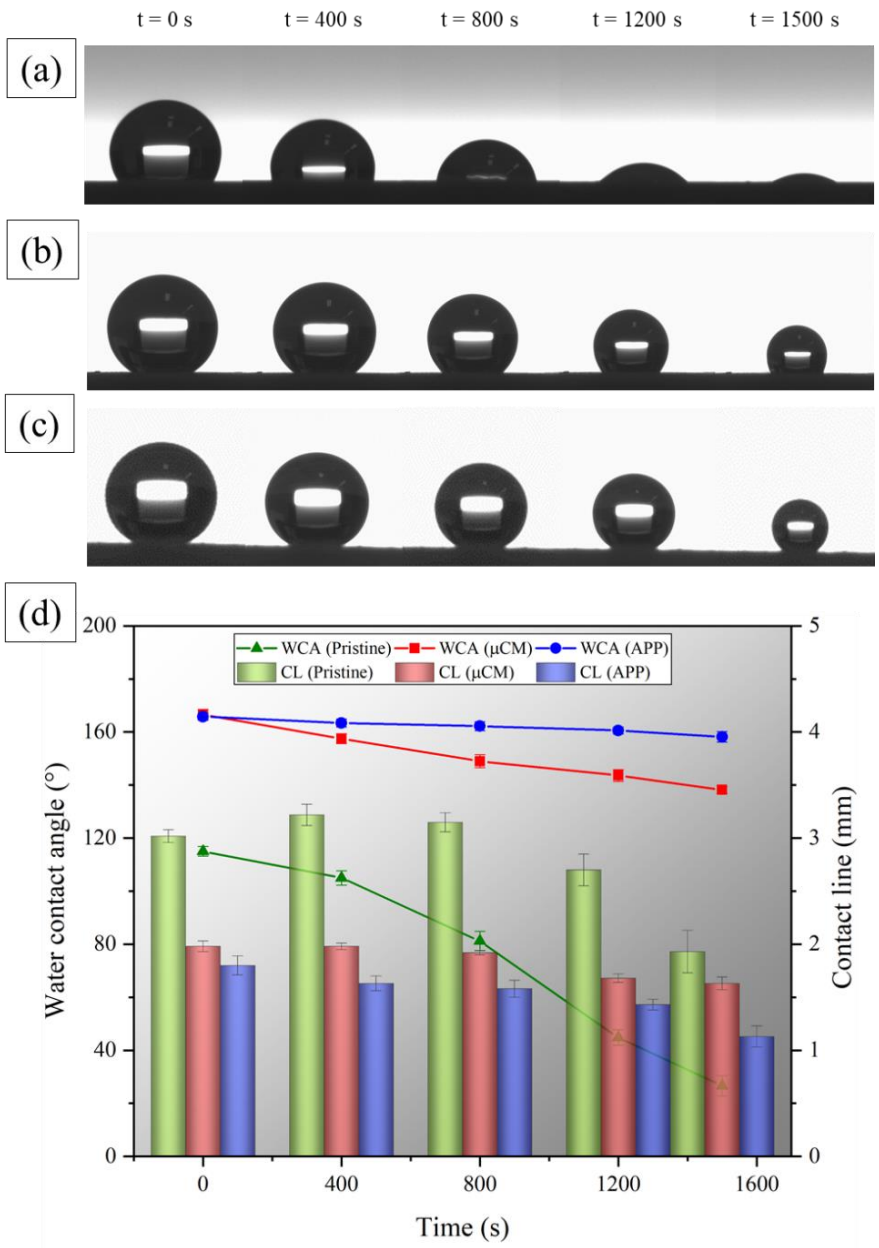

Fig. 4. Images of droplet evaporation on (a) pristine, (b) μCM, and (c) APP-treated silicone rubber surfaces. (d) Changes to the water contact angle and contact line over time for each surface.

3.2. Icephobic properties

In the development of icephobic surfaces, two main properties are usually considered: anti-icing and de-icing. Anti-icing refers to a property of surface to delay or reduce ice accretion, whereas the de-icing approach is attributed to the removal of formed ice on the surface. The anti-icing property of the produced surfaces was examined through the measurement of the WCA at below-zero temperatures and the freezing

delay. The de-icing property, however, was examined using measurements of the ice adhesion strength based on the centrifuge and push-off tests.

3.2.1. Anti-icing properties

To assess the behavior of the produced surfaces at supercooled temperatures, we measured the variation of WCA at various temperatures (Fig. 5 (a)). The WCA decreased for all surfaces at below-zero temperatures. Maghsoudi et al. (2018) ascribed this decrease to the surface tension of water at low temperatures. Behroozi et al. (2011) showed that at low temperatures, the surface tension of the water droplets strengthens, thus leading to an increase in the internal pressure of a droplet and may provoke a transition from a Cassie-Baxter to a Wenzel regime. The APP-treated surface displayed a relatively higher WCA than that of the µCM surface at freezing temperatures. This difference can be related to the better functionality of the lower surface roughness on the APP-treated surface compared to µCM surface roughness in the Cassie-to-Wenzel transition at freezing temperatures. A close inspection of the curve slope of each surface revealed that the WCA of the APP-treated surface decreased slower than that of the WCA for the µCM surface. So, the WCA of the APP-treated surface remained >150° even at -15 °C, while the WCA of the µCM surface was <150° at -10 °C. However, below -15 °C, the WCA of both surfaces decreased almost monotonically due to the increased internal pressure of the droplet and a possible wetting regime transition.

We also present the results of freezing delay for three temperatures: -15 °C, -20 °C, and -25 °C (Fig. 5 (b)). We did not consider the freezing delays at -5 °C and -10 °C given that they were too long for this experiment. We observed a marked delay in freezing on the superhydrophobic surfaces due to the existence of micro-nanostructures when compared to the pristine surfaces, which lack these structures. As an initial explanation of such behavior is the reduced contact area between the water droplet and the surfaces when WCA is high. As such, the thermal conductivity decreased dramatically for superhydrophobic surfaces compared to the pristine surface. In addition, Maghsoudi et al. (2020) observed that the delay in freezing time mainly stemmed from the micro air cushions trapped in the surface micro-nanostructures to therefore act as a thermal barrier. Consequently, the creation of micro-nanostructures on the superhydrophobic surfaces led to less heat dissipation than observed from the smooth pristine surface. Therefore, the greater the volume of trapped air cushions, the longer the freezing delay. Using the profilometry technique, we determined that, compared to the pristine surface, the µCM and APP-treated surfaces entrapped 14.2× and 4.7× more air, respectively, within their surface structures. At -15 °C, the µCM surface showed a ~40% greater delay in freezing time compared to the APP-treated surface that had a relatively greater abundance of nanostructures. This difference was most significant at -25 °C. As for the µCM surface, the freezing delay time was ~2.5× greater than that of the APP-treated surface. This illustrates that surface roughness has a more considerable contribution to the freezing process at lower temperatures. The videos of the water

droplet freezing process on the pristine surfaces and superhydrophobic surfaces are provided (Supplementary Information).

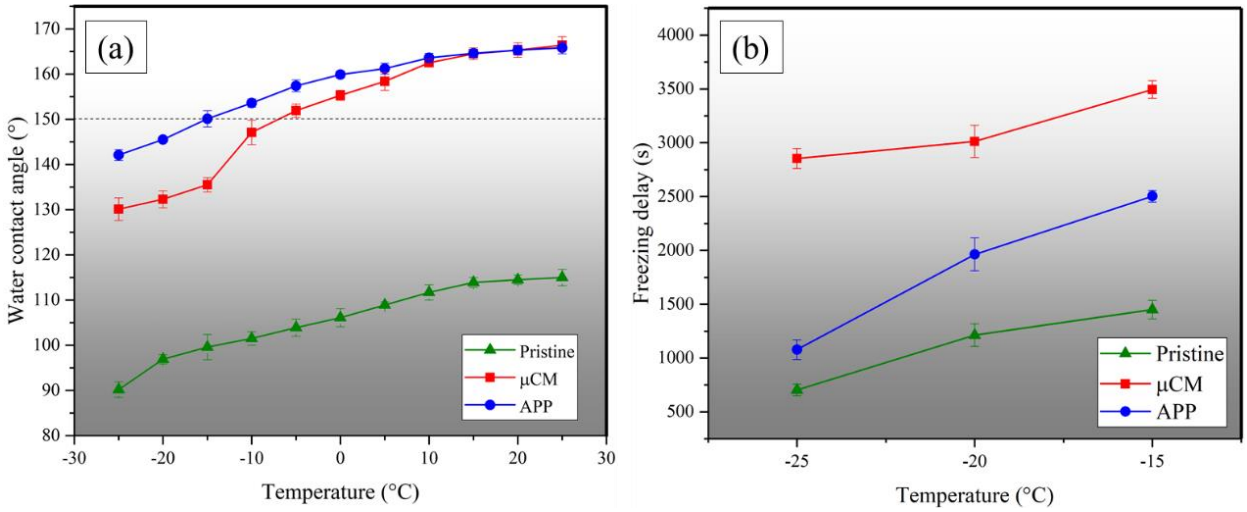

Fig. 5. (a) Variation in water contact angle and (b) freezing delay at various temperatures for the pristine, µCM, and APP-treated surfaces (the dashed line in (a) shows the threshold of superhydrophobicity).

3.2.2. De-icing properties

Through the push-off test, both superhydrophobic surfaces reduced ice adhesion strength. While de-icing of the pristine surface required a pressure of 132.8 kPa, the µCM and APP-treated surfaces required only 90.1 kPa and 32.9 kPa, respectively, to become de-iced during the first icing/de-icing cycle (Fig. 6 (a)). The energy required for de-icing the pristine surface was ~30 mJ, whereas the µCM and APP-treated surfaces required only 8.75 mJ and 0.51 mJ, respectively (Fig. 6 (b)). Regarding the shape of the produced curves (Fig. 6 (b)), it can be concluded that the pristine and µCM surfaces showed the same behavior when de-icing. Zou et al. (2011) called this behavior as the plastic deformation of ice. In this case, the applied force to the ice pillar increases gradually until the force overcomes the adhesion force between the ice and top of the surface structures and detaches the interlocked ice from the surface asperities. According to Maghsoudi et al. (2020), the lower liquid-solid contact area, which is corresponded to higher WCA, results in less ice-surface contact area, thereby reducing the force required for ice detachment from the surface. Therefore, the lower force required for the µCM surface, compared to the pristine surface, is related to the lower ice-surface contact area due to the higher WCA of the µCM surface. However, the APP-treated curve showed a very different behavior, i.e., elastic deformation. A sudden jump in the curve was observed at the de-icing point showing that the amount of interlocked ice was negligible. Zou et al. (2011) observed that the applied force was only required to overcome the adhesion of ice to the top of the features. Thus, there is a similarity

between the de-icing behavior of the pristine and μCM surfaces, a behavior that is in sharp contrast with that of the APP-treated surface.

The push-off test was repeated seven times on each surface to assess the durability of the surfaces under repetitive icing/de-icing cycles. The ice adhesion strength of the μCM surface did not necessarily increase (Fig. 6 (c)), and in some cases, ice adhesion strength was even lower after the first cycle of the test, e.g., cycles 2 and 5. This testifies to the durability of the μCM surface micro-nanostructures during the de-icing process. The ice adhesion strength of the APP-treated surface, on the other hand, increased gradually after the 4^{th} cycle, related to the removal of nanostructures during ice detachment (discussed in detail below).

We observed almost identical trends when the centrifuge tests assessed ice-covered surfaces under conditions of freezing drizzle (Fig. 6 (d)). The pristine silicone rubber surface showed an ice adhesion strength of about 120 ± 3.6 kPa; both superhydrophobic surfaces reduced the ice adhesion strength. The adhesion strength of the μCM surface did not significantly increase (even at the 6^{th} cycle, the ice adhesion strength remained low), while that of the APP-treated surface increased significantly through the seven icing/de-icing cycles. Thus, ice adhesion to the μCM surface depended highly on the probability that ice interlocked into the surface structures, while the increased ice adhesion strength of the APP-treated surface stemmed from the gradual deterioration of nanostructures. The SEM images of the surfaces after the 7^{th} icing/de-icing cycle are shown in Fig. S1.

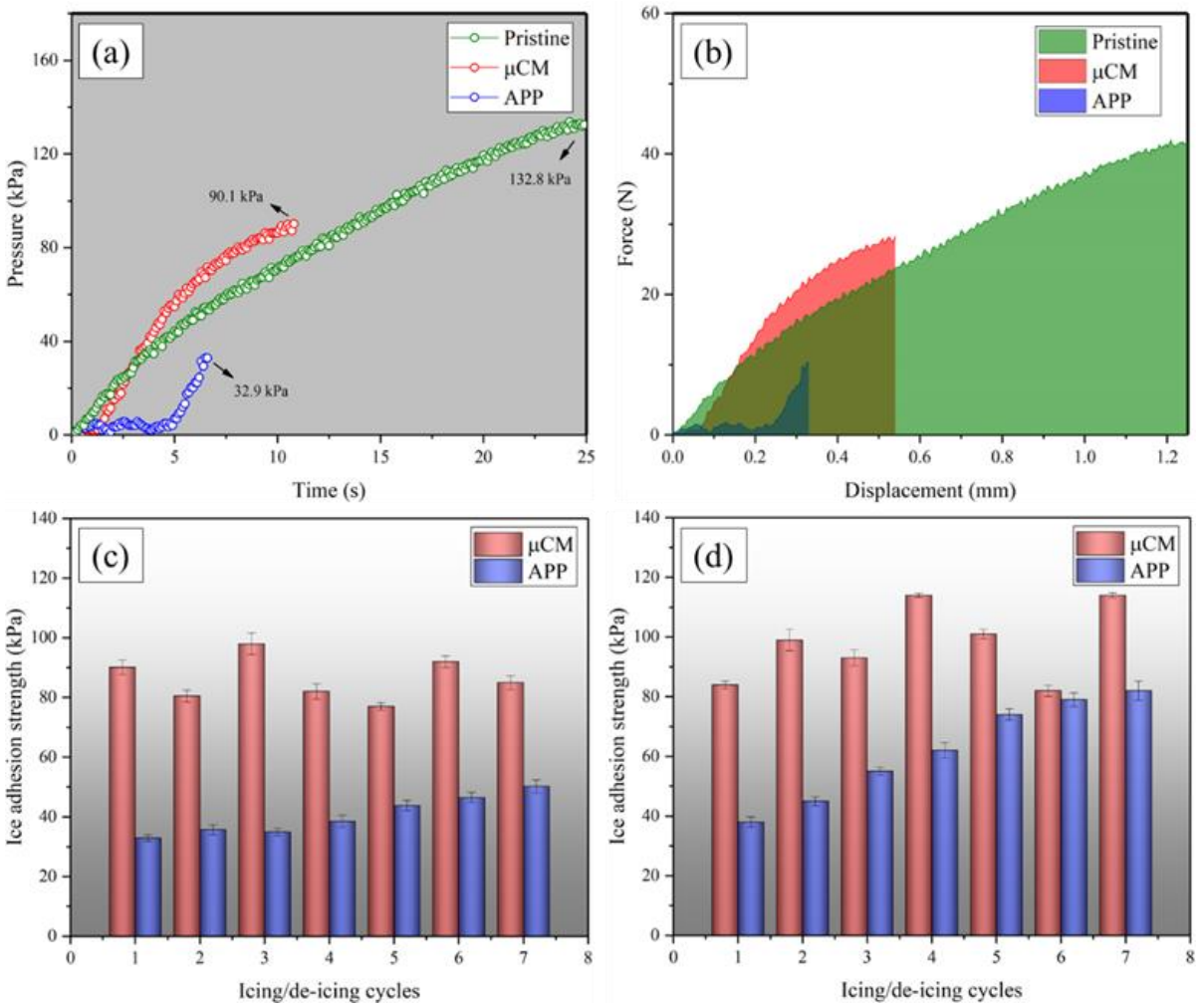

Fig. 6. (a) De-icing pressure required for surfaces in the push-off test and (b) the corresponding de-icing energy of each surface. Ice adhesion strength for repetitive icing/de-icing cycles for the (c) push-off and (d) centrifuge tests.

Compared to the pristine silicone rubber surface, ice adhesion reduction varied between ~26% and ~42% for the µCM surface and decreased ~75% to ~62% for the APP-treated surface over seven icing/de-icing cycles in the push-off test (Table 2). In the centrifuge test, the ice adhesion strength decreased ~30% for the µCM surface and ~68% for the APP-treated surface after the first cycle (Table 2). The APP-treated surface showed a better de-icing property at each cycle although also showed a significant loss of its de-icing properties, whereas the µCM surface exhibited a lower reduction in ice adhesion but showed a greater durability against repetitive icing/de-icing cycles. The ice adhesion reduction factor (ARF) values—usually reported according to the ice adhesion strength of bare aluminum—offer a better understanding of the de-icing properties of the produced surfaces (Table S1).

In terms of the de-icing properties of surfaces having hierarchical micro-nanostructures, surfaces having a lower surface roughness produced a lower ice adhesion. This relates to the interlocking of ice into the surface structures, which can result in enhanced adhesion strength. Davis et al. (2014) observed that among three surfaces having arithmetic mean surface roughness values of 8.7 µm, 2.7 µm, and 1.6 µm, the lowest ice adhesion strength was obtained for the surface having the lowest surface roughness. A comparison of the root mean square height (S_q) of the µCM and APP-treated surfaces (9.40 µm and 1.53 µm, respectively) confirms this observation. However, higher surface roughness can improve surface durability against repetitive icing/de-icing cycles.

Table 2. The ice adhesion reduction values for the µCM and APP-treated surfaces during the push-off and centrifuge tests.

Ice adhesion reduction (%)	**Icing/de-icing cycles**		**1**	**2**	**3**	**4**	**5**	**6**	**7**
	push-off	µCM	32.3 ± 1.9	39.5 ± 2.3	26.3 ± 2.9	38.3 ± 1.9	42.1 ± 2.3	30.8 ± 1.9	36.1 ± 1.7
		APP	75.3 ± 1.7	73.2 ± 1.9	73.8 ± 2.6	71.0 ± 1.9	67.1 ± 1.3	65.0 ± 2.3	62.2 ± 1.7
	centrifuge	µCM	30.0 ± 1.3	17.5 ± 3.6	22.5 ± 2.7	15.0 ± 0.7	15.8 ± 1.6	31.7 ± 1.9	15.0 ± 0.7
		APP	68.3 ± 1.7	62.5 ± 1.5	54.2 ± 1.3	48.3 ± 2.6	38.3 ± 1.9	34.2 ± 2.3	30.8 ± 3.3

The differing results of the two measurement methods for ice adhesion (push-off test and centrifuge test) may stem from a difference between the type of ice formed in each test. In the push-off test, a non-impact bulk ice forms on the surface by deposition of a water pillar on the surface, and the icephobic behavior of the surfaces depends highly on the Cassie-Baxter consistency during the icing process. If the micro-nanostructures hinder water to penetrate into the surface asperities before icing, a non-interlocked ice (Cassie ice) can form on the surface and produce a low ice adhesion strength. However, in the centrifuge test, the surfaces were covered with glaze ice produced by freezing drizzle; freezing drizzle represents one of the most severe icing conditions where the supercooled microdroplets can penetrate the surface structures. Therefore, the ice adhesion strength in the centrifuge test depended highly on the icing condition parameters, particularly the MVD. The APP-treated surface, with reduced surface roughness, resisted the penetration of water microdroplets (size of 324 µm), whereas the water microdroplets could penetrate partially into the µCM surface structures producing a higher ice adhesion strength. The WCA and CAH of the produced surfaces were measured after the 7^{th} cycle of icing/de-icing in both the push-off and centrifuge tests (Table S2). Both surfaces presented a high WCA and low CAH to demonstrate the stability of water

repellency after multiple icing/de-icing cycles. The photographs of each surface at the 1st and 7th icing/de-icing cycles after ice accumulation and ice removal in the centrifuge test are presented in Fig. S2. In the 1st cycle, the spherical shape of supercooled water droplets freezing on the superhydrophobic surfaces highlighted the water-repellent property at a freezing temperature. This was not observed for the pristine surface. The rounded shape of the formed ice on the APP-treated surface at the 7th cycle illustrated its most favorable water-repellent property.

3.3. Durability property

We investigated the durability of the produced superhydrophobic surfaces through various mechanical and chemical tests that represent the real-life applications, including abrasion using sandpaper, a finger-press test, a tape-peeling test, sandstorm simulation, ultrasonication treatment, continuous water droplet impacts, immersion in chemical solutions, and exposure to UV-light radiation. We closely monitored and recorded the WCA and CAH of the samples to study the capacity of a surface to recover its superhydrophobicity, where applicable.

3.3.1. Mechanical durability

The sandpaper abrasion test of superhydrophobic surfaces is effective for evaluating mechanical durability; however, studies often stop abrasion cycles before any deterioration of superhydrophobicity. Here, we maintained the cycles once the superhydrophobic properties began to deteriorate to provide a thorough understanding of mechanical stability. The superhydrophobic properties of the µCM surface were not lost (WCA >150°) even after 300 abrasion cycles for abrasion pressures of 1.6 kPa and 3.2 kPa (Fig. 7). However, the CAH increased to >10° after 250 cycles. Under these same conditions, i.e., abrasion pressures of 1.6 kPa and 3.2 kPa, the WCA of the APP-treated surfaces fell below 150° after 200 and 150 cycles, respectively. The CAH became >10° after 100 cycles. Increasing the abrasion pressure to 6.4 kPa, which is a relatively high pressure for any abrasion test, the µCM surface maintained its WCA >150° after 200 cycles, whereas the APP-treated surface showed a WCA <150° after 100 cycles. The CAH of the µCM surface increased to >10° after 100 cycles, whereas that of the APP-treated surface showed a CAH of ca. 20° after 50 cycles. This observation relates to the fast deterioration of surface micro-nanostructures under such high abrasion pressure.

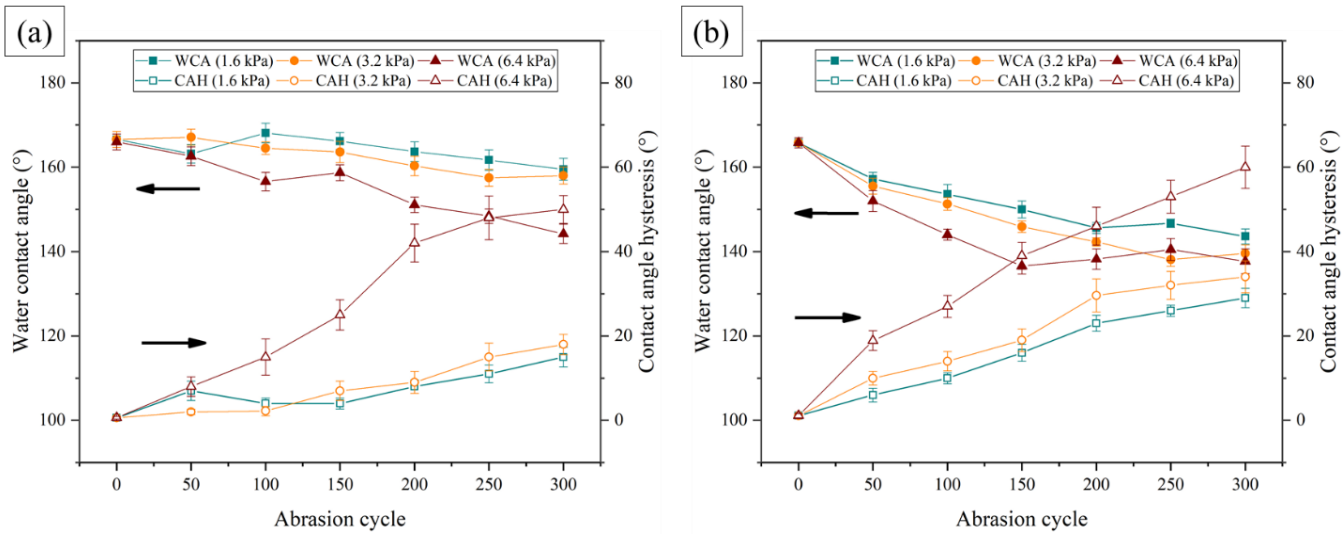

Fig. 7. WCA and CAH as a function of abrasion cycles using various abrasion pressures for (a) µCM and (b) APP-treated surfaces.

SEM images of the surfaces after being abraded for 300 cycles using sandpaper (Fig. 8) illustrate the decreased micro-nanostructures on the surface after the abrasion process. When comparing surfaces abraded using pressures of 3.2 kPa and 6.4 kPa, we observed that the greater the abrasion pressure, the more the surface asperities wore out. Higher abrasion pressures produced flatter surfaces and removed the microstructures. The red outlines in Fig. 8 illustrate areas where structures were lost due to abrasion, while the yellow outlines denote areas where the structures remained intact or less severely damaged. A greater number of yellow areas are present in samples subjected to 3.2 kPa abrasion pressures, explaining the relatively high WCA, whereas the greater number of red shapes in the sample abraded at 6.4 kPa indicates the flattened structures and, therefore, explains the reduced WCA and increased CAH.

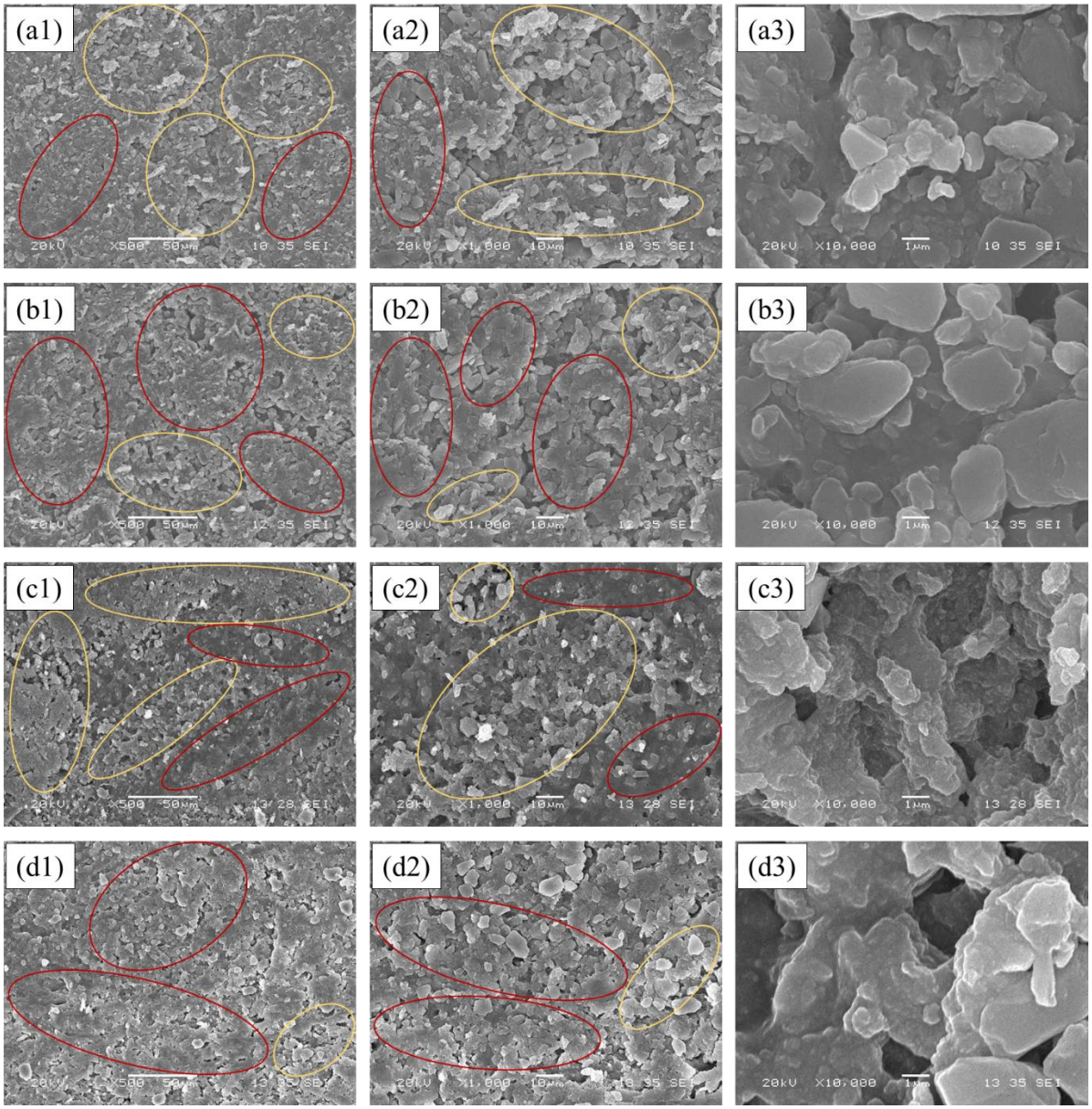

Fig. 8. SEM images at various magnifications of (a1-a3) µCM surface abraded at 3.2 kPa pressure, (b1-b3) µCM surface abraded at 6.4 kPa pressure, (c1-c3) APP-treated surface abraded at 3.2 kPa pressure, and (d1-d3) APP-treated surface abraded at 6.4 kPa pressure.

We measured the WCA of both surfaces abraded at 6.4 kPa at regular intervals to determine the recovery of surface superhydrophobicity (Fig. S3 (a)). The WCA of the µCM surface increased constantly up to 20 days after the tests, and it thereafter remained unchanged at the value of ~157°. For the µCM surface (an initial WCA of 166.6°), the recovery capability of the silicone surface was significant. The WCA of the APP-treated surface (an initial WCA of 165.8°), however, showed a slight increase after the first 10 days post-test and then remained at an almost constant value of ~143°, showing non-superhydrophobic behavior. During the abrasion test, the asperities may undergo two changes. First, the microstructures and

nanostructures are worn out as they are vulnerable to abrasion. This type of deformation is not reversible, which explains the permanent deterioration of CAH—CAH did not change considerably after the tests and remained >10° even after 50 days of rest for both prepared surfaces. Second, as the complete wearing of microstructures is less possible than the full loss of nanostructures, the microstructures are bent and stretched under pressure and drag forces. Therefore, there is a possibility of recovery due to the elastic properties of silicone rubber asperities, where microstructures can return upright and recover their initial position with time.

We also examined the durability of the produced silicone rubber surfaces via a finger-press test where we applied a pressure of 80 ± 8.8 kPa to the surfaces using a bare thumb (Fig. 9 (a)). This test can mimic human handling of a material to test whether a superhydrophobic surface can be suitable for commercial application. In addition to mechanical damage, a bare finger-press also adds salt and oil contaminants to the surface. Therefore, the finger-press test can both physically and chemically affect a superhydrophobic surface. In our finger-press tests, the µCM surfaces degraded more than the APP-treated surfaces. Although the WCA of both surfaces decreased almost similarly and remained at >150° after 50 cycles (APP-treated showed a slightly more durable behavior), the CAH of the µCM surfaces increased markedly after 10 cycles, whereas the CAH of the APP-treated surface remained <10° even after 50 finger-press cycles.

The increase in WCA after a single day of recovery following the finger-press test was an important result (Fig. S3 (b)). The WCA of the finger-pressed µCM surface increased from 148.5° to 164.2°, while the WCA of the APP-treated surface increased from 152.8° to 155.9°. The micro-nanostructured silicone asperities could therefore return to their initial position after the finger force was released due to the rubber elasticity. These post-pressure behaviors are explained by the different micro-nanostructures on the surfaces. A portion of the WCA loss can also be attributed to the added salt and oil contaminant from thumb to the surface. As such, some of the observed WCA recovery can be related to the migration of LMWS to the surface and covering the contamination molecules transferred to the surface by the thumb. Finally, after 10 days of recovery, the CAH of the µCM surface attained 9° (while the graph plateaued after Day 8). The CAH of the APP-treated surface did not show any significant change.

The tape-peeling test involved applying and removing a pressure-sensitive Scotch-600 tape with approximately 30 kPa pressure to the surface. In terms of the pressure placed onto the surface, this test combines the effects of the finger-press test and the adhesion test, as though the sample underwent 50 cycles of the finger-press test and tape-peeling test simultaneously. After 50 attach-detach cycles, both surfaces remained superhydrophobic with a WCA >160° and a CAH < 6° (Fig. 9 (b)).

In ultrasonication, the energy is applied by waves at an ultrasonic frequency (>20 kHz) within a liquid media. Milionis et al. (2016) observed that this energy can damage a surface lacking a strong physical morphology or a strong chemical bonding with the substrate. The μCM surface was durable against long-term ultrasonication. After 4 h of continuous ultrasonication, the WCA of the μCM surface remained at ~160° and the CAH was at ~10° (Fig. 9 (c)), confirming the strong physical micro-nanostructured morphology of the prepared superhydrophobic surface. The APP-treated surface, however, was significantly vulnerable to ultrasonication. The WCA of the APP surface dropped below 150° after 60 min and was ~124° after 4 h. The CAH increased to >20° after 60 min and to ~60° after 4 h. This marked change occurs as nanostructures are removed from the APP-treated surface by the high levels of applied ultrasonic energy (Fig. S4).

We investigated the dynamic impact durability of the superhydrophobic surfaces under a liquid phase. This evaluation is very important in terms of the application of produced superhydrophobic surfaces under rain precipitation. We conducted this test at a flow rate of ~1 $mL \cdot min^{-1}$ and we ran the test for 7000 seconds, i.e., ~120 mL water impacting a single point of the surface at a speed of 1.4 $m.s^{-1}$. According to van Boxel (1997) measurements, this speed was equivalent to that of 3.0-mm diameter raindrops. The WCA and CAH remained >150° and <10° after being exposed to a water jet impact, i.e., ~6000 droplet impact events, after 7000 s (Fig. 9 (d)). Milionis et al. (2016) ascribed the reduction of the anti-wetting properties to the partial penetration of water into the surficial hierarchical structures due to the instantaneous pressure exerted on the surface.

The dynamic impact durability of the produced superhydrophobic surfaces under a solid phase was also examined. We simulated sandstorm conditions (average particle size of 18 μm) in a sandblasting machine. Each individual surface was exposed to the sand stream at a pressure of 20 psi for 20 min, and we recorded the WCA and CAH every 5 min (Fig. 9 (e)). Both surfaces showed a WCA >150° and a CAH <10° after 20 min of sandblasting (corresponding to a full year of real-life sandstorm events). The SEM images of the sandblasted surfaces are shown in Fig. S5.

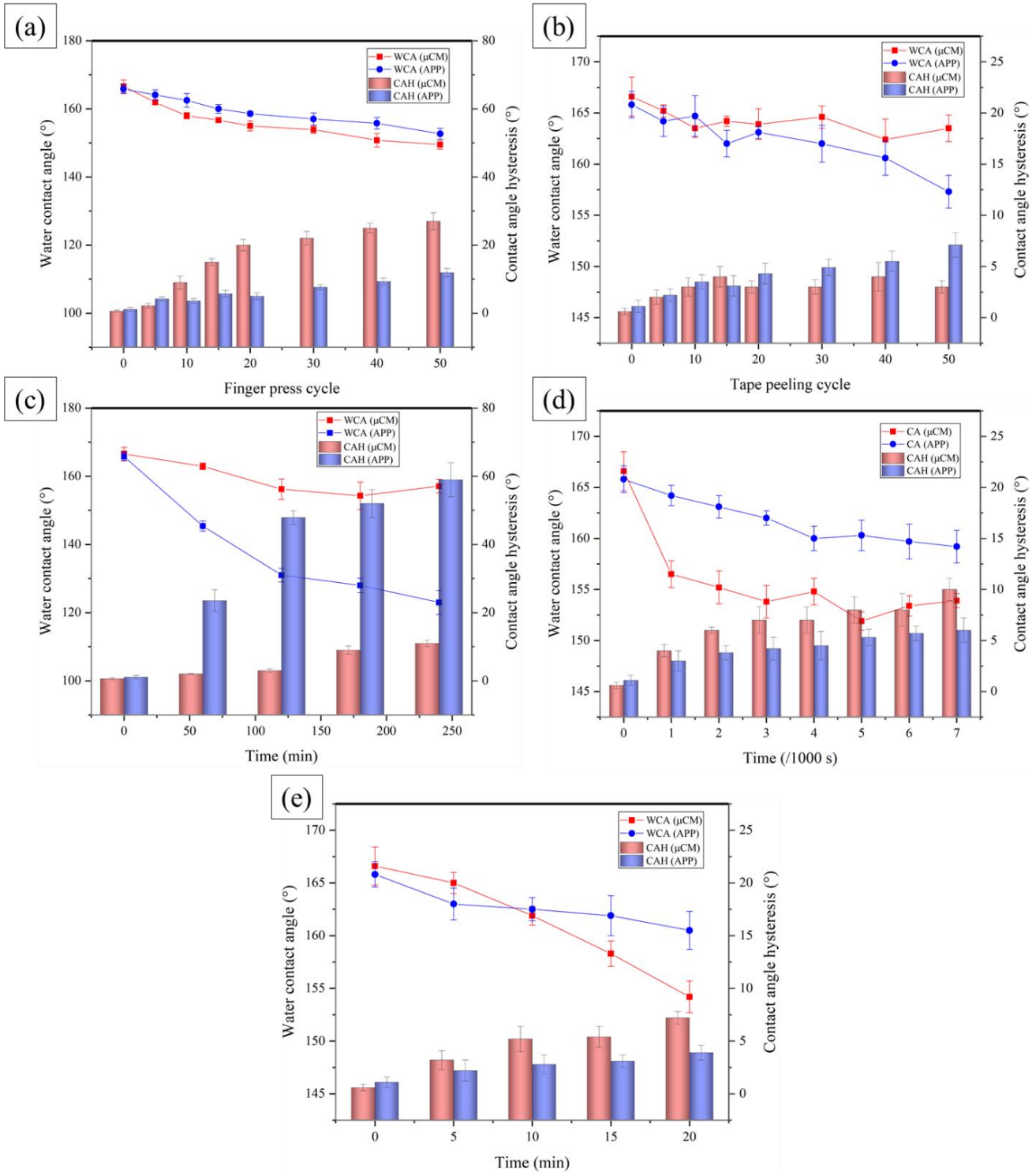

Fig. 9. WCA and CAH as a function of (a) finger-press cycle, (b) attach-detach cycle, (c) ultrasonication time, (d) continuous water droplet impact time, and (e) sandblasting time for μCM and APP-treated surfaces.

3.3.2. Chemical durability

We then tested the durability of the produced superhydrophobic surfaces against buffer solutions of pH 2, pH 12, and deionized water of pH 7. When superhydrophobic surfaces are immersed in aqueous solutions, there are two possibilities for deterioration of superhydrophobic behavior. One possibility is related to the penetration of liquid into the surface structures (Cassie-to-Wenzel transition) which is mainly dominated by capillary forces. Papadopoulos et al. (2018) showed that the morphology of the surface structures determines the capillary forces dominating the penetration of the droplet into the surface structures. The other possibility, however, is related to the formed chemical bonds due to the presence of aqueous medium.

After 15 days of immersion in the acidic solution, the WCA of the µCM surface remained >155°, while the CAH increased to 12°; thus, the surface was superhydrophobic with a weak roll-off property (Fig. 10 (a)). The µCM surface in the alkaline solution had a WCA remaining at >160° and a CAH remaining at <5°. The WCA of the µCM surface was >150° and the CAH increased to 30° after 15 days of water immersion. These observations can be attributed to the creation of oxide/hydroxide groups in the vicinity of the solutions for an extended period of time. On the µCM surface, the silicone rubber chains, as well as the ATH particles, react with the acid, base, and water to produce these oxide/hydroxide groups.

The APP-treated surface demonstrated extraordinary durability against the three aqueous media. A WCA >160° and CAH <5° testified to a desirable chemical durability of the APP-treated surface (Fig. 10 (b)). Wang et al. (2018) showed that the APP process at elevated temperatures breaks the chemical bonds of the silicone rubber chains, and therefore the surface is mainly covered by silicon oxide. These SiO_2 do not react with the acidic, alkaline, and neutral water media. As such, the SiO_2 acts as a shield to prevent chemical reactions on the APP-treated surface. Moreover, according to Kim et al. (2018) the capillary pressure, corresponding to the pressure that resists water penetration, is inversely related to the structure gap ($P_c = 2\sigma.cos\theta/r$, where σ is liquid surface tension, θ is the intrinsic contact angle of the surface, and r is the distance between the surface structures). Therefore, on the immersed surfaces, the smaller micro-nanostructures having greater capillary force can hinder the Cassie-to-Wenzel transition. This is witnessed by lower reduction of WCA on the APP-treated surface.

Due to the migration of LMWS molecules from the bulk material to the surface and the reorientation of methyl and hydroxyl groups by conformational changes, the optimal WCA and CAH conditions were recovered (Fig. S3 (c)). The LMWS chains that are thermodynamically driven to the surface minimized the

surface free energy. Therefore, this restoration was resulted from the rotation and movement of the LMWS chains at the surface.

As the sunlight radiation is a major destructive force, the durability of silicone surfaces used for outdoor applications, e.g., electrical insulation, exposed to UV radiation is of great importance. The sun emits ultraviolet, visible light, and infrared waves, ultraviolet waves being the most destructive. The WCA and CAH of the superhydrophobic surface remained >150° and <10° respectively after being exposed to 1200 h of UV light, representing about six years under natural conditions (Fig. 10 (c)) (the calculations are provided in Supplementary Information). The produced surfaces thus demonstrated resistance against accelerated UV-light exposure. The better performance of the APP-treated surface over that of the μCM surface is due to the silicon oxide layer formed on the surface acting as a shield against UV-light exposure.

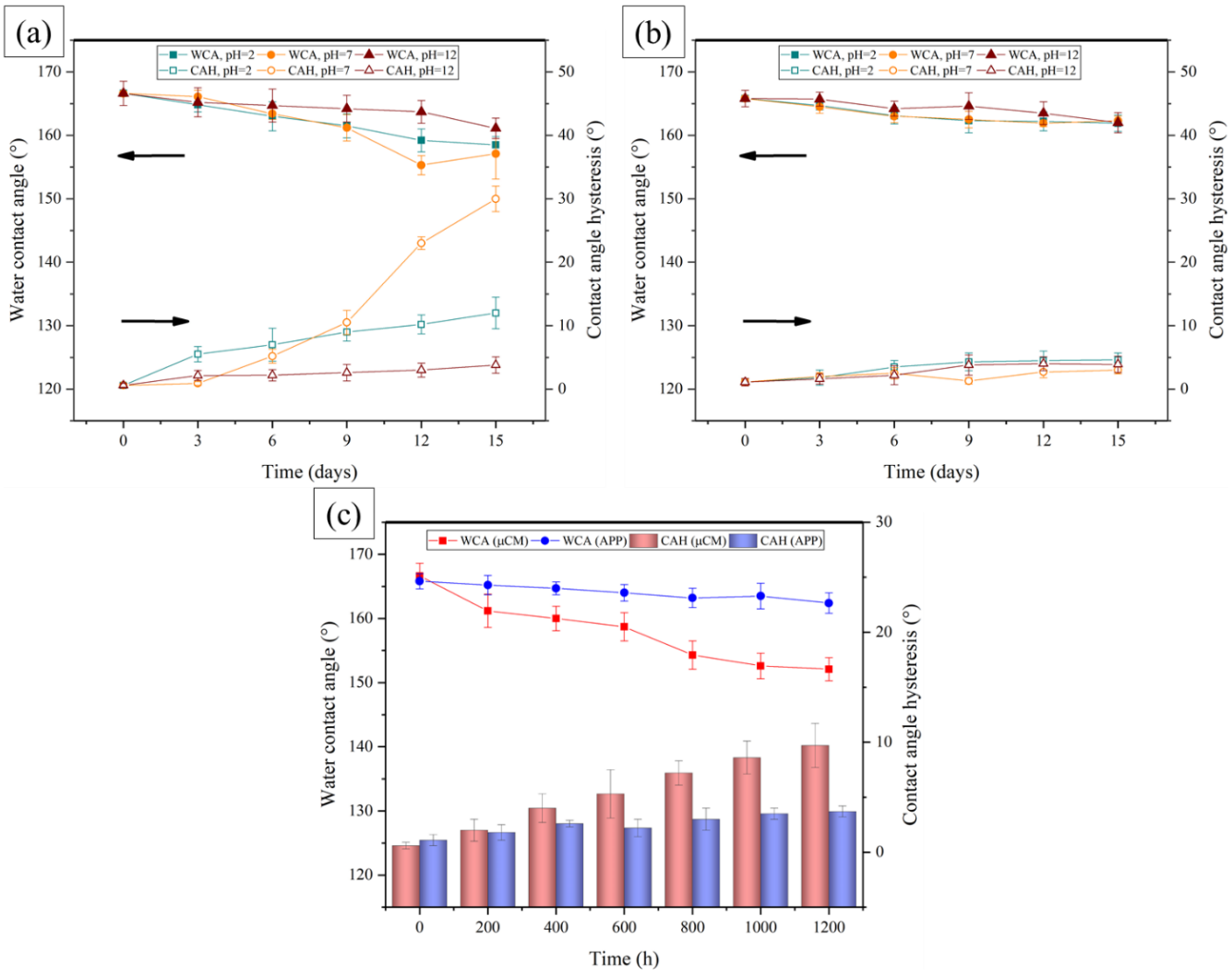

Fig. 10. WCA and CAH as a function of immersion time (days) in acidic, alkaline, and neutral solutions for (a) μCM and (b) APP-treated surfaces. (c) WCA and CAH as a function of UV-light exposure time for μCM and APP-treated surfaces.

3. Conclusions

We fabricated superhydrophobic silicone rubber surfaces having a WCA >150° and a CAH <10° via straightforward direct replication method using a micro compression molding (μCM) system and a simple treatment by atmospheric pressure plasma (APP). The icephobic properties of the produced surfaces were assessed with the aim of the study of various surface micro-nanostructures created by each method. The observed delay in the freezing time of droplets on the produced superhydrophobic surfaces stemmed from the creation of air cushions on their surfaces. The larger micro-nanostructures showed better anti-icing properties as they could trap more air within their micro air cushions. As for the μCM surface, the freezing

delay time was ~2.5× more than that of APP-treated surface at –25 °C. Using centrifuge and push-off tests—with corresponding icing conditions of glaze and bulk ice, respectively—we demonstrated that the produced superhydrophobic surfaces also decreased ice adhesion strength. The mechanism of ice removal for the µCM and the pristine surface was the plastic deformation of ice, while elastic deformation controlled ice removal from the APP-treated surface. Compared to a pristine silicone rubber, the APP-treated surface (S_q = 1.53 µm) decreased the ice adhesion strength up to 75% in a push-off test and 68% in a centrifuge test, whereas the µCM surface (S_q = 9.40 µm) reduced ice adhesion strength up to 42% in a push-off test and 32% in a centrifuge test. Therefore, for surfaces having hierarchical micro-nanostructures, those surfaces with a lower surface roughness are characterized by a lower ice adhesion strength. The stronger physical bonding between the micro-nanostructures and the bulk material in the µCM surface, however, led to a relatively constant ice adhesion strength throughout repetitive icing/de-icing cycles. The durability of the produced silicone rubber superhydrophobic surfaces were tested through mechanical and chemical experiments. The samples showed desirable durability properties maintaining a WCA of >150° and a CAH of <10° in several tests. Silicone rubber materials also showed a self-repair capacity stemming from the elasticity of the rubber and migration of LMWS to the surface. This recovery compensated for the loss of anti-wetting properties in some destructive tests, and the WCA recovered after a couple of days. There remains an enticing study on the chemical origin of the contribution of LMWS to the recovery of anti-wetting properties of silicone rubbers.

4. Acknowledgments

We acknowledge the financial support from the Natural Sciences and Engineering Research Council of Canada (NSERC) and K-Line Insulators Limited, Toronto, Canada. We also thank the Anti-icing Materials International Laboratory (LIMA) for carrying out the centrifuge adhesion tests.

5. References

Alizadeh, A., Yamada, M., Li, R., Shang, W., Otta, S., Zhong, S., Ge, L., Dhinojwala, A., Conway, K. R. and Bahadur, V., 2012. Dynamics of ice nucleation on water repellent surfaces. Langmuir 28(6): 3180-3186.

Behroozi, F. and Behroozi, P., 2011. Determination of surface tension from the measurement of internal pressure of mini soap bubbles. Am. J. Phys. 79(11): 1089-1093.

Cansoy, C. E., Erbil, H. Y., Akar, O. and Akin, T., 2011. Effect of pattern size and geometry on the use of Cassie–Baxter equation for superhydrophobic surfaces. Colloids Surf., A 386(1-3): 116-124.

Chu, D., Nemoto, A. and Ito, H., 2014. Enhancement of dynamic wetting properties by direct fabrication on robust micro–micro hierarchical polymer surfaces. Appl. Surf. Sci. 300: 117-123.

Dash, S. and Garimella, S. V., 2013. Droplet evaporation dynamics on a superhydrophobic surface with negligible hysteresis. Langmuir 29(34): 10785-10795.

Davis, A., Yeong, Y. H., Steele, A., Bayer, I. S. and Loth, E., 2014. Superhydrophobic nanocomposite surface topography and ice adhesion. ACS Appl. Mater. Interfaces 6(12): 9272-9279.
Eberle, P., Tiwari, M. K., Maitra, T. and Poulikakos, D., 2014. Rational nanostructuring of surfaces for extraordinary icephobicity. Nanoscale 6(9): 4874-4881.
Fortin, G. and Perron, J., 2012. Ice adhesion models to predict shear stress at shedding. J. Adhes. Sci. Technol. 26(4-5): 523-553.
Ghalmi, Z. and Farzaneh, M., 2015. Experimental investigation to evaluate the effect of PTFE nanostructured roughness on ice adhesion strength. Cold Reg. Sci. Technol. 115: 42-47.
Golovin, K., Boban, M., Mabry, J. M. and Tuteja, A., 2017. Designing Self-Healing Superhydrophobic Surfaces with Exceptional Mechanical Durability. ACS Appl. Mater. Interfaces 9(12): 11212-11223.
He, Y., Jiang, C., Cao, X., Chen, J., Tian, W. and Yuan, W., 2014. Reducing ice adhesion by hierarchical micro-nano-pillars. Appl. Surf. Sci. 305: 589-595.
Hillborg, H., Sandelin, M. and Gedde, U. W., 2001. Hydrophobic recovery of polydimethylsiloxane after exposure to partial discharges as a function of crosslink density. Polymer 42(17): 7349-7362.
Huang, L., Zhang, L., Song, J., Wang, X. and Liu, H., 2020. Superhydrophobic Nickel-Electroplated Carbon Fibers for Versatile Oil/Water Separation with Excellent Reusability and High Environmental Stability. ACS Appl. Mater. Inter. 12(21): 24390-24402.
Jafari, R., Momen, G. and Farzaneh, M., 2016. Durability enhancement of icephobic fluoropolymer film. J. Coat. Technol. Res. 13(3): 405-412.
Khedir, K. R., Kannarpady, G. K., Ishihara, H., Woo, J., Trigwell, S., Ryerson, C. and Biris, A. S., 2011. Advanced studies of water evaporation kinetics over teflon-coated tungsten nanorod surfaces with variable hydrophobicity and morphology. J. Phys. Chem. C 115(28): 13804-13812.
Kim, H. and Kim, S. H., 2018. Nonwettable hierarchical structure effect on droplet impact and spreading dynamics. Langmuir 34(19): 5480-5486.
Lazauskas, A., Guobienė, A., Prosyčevas, I., Baltrušaitis, V., Grigaliūnas, V., Narmontas, P. and Baltrusaitis, J., 2013. Water droplet behavior on superhydrophobic SiO2 nanocomposite films during icing/deicing cycles. Mater. Charact. 82: 9-16.
Li, J., Zhou, X., Zhang, Y., Hao, C., Zhao, F., Li, M., Tang, H., Ye, W. and Wang, Z., 2020. Rectification of mobile Leidenfrost droplets by planar ratchets. Small 16(9): 1901751.
Li, Q. and Guo, Z., 2018. Fundamentals of icing and common strategies for designing biomimetic anti-icing surfaces. J. Mater. Chem. A 6(28): 13549-13581.
Ling, E. J. Y., Uong, V., Renault-Crispo, J.-S. b., Kietzig, A.-M. and Servio, P., 2016. Reducing ice adhesion on nonsmooth metallic surfaces: wettability and topography effects. ACS Appl. Mater. Interfaces 8(13): 8789-8800.
Liu, H., Cash, G. A., Sovar, R. D., George, G. A. and Birtwhistle, D., 2006. Studies of the diffusion of low molecular weight silicone fluids on polluted hv silicone insulators. I. use of diffuse reflectance FTIR. IEEE Transactions on Dielectrics Electrical Insulation 13(4): 877-884.
Liu, Y., Cai, W., Gao, S., Yao, T., Huang, D., Chen, Y. and Xu, Z., 2012. Study of the effect of ice adhesion on electrical power transmission insulator. J. Adhes. Sci. Technol. 26(4-5): 593-602.
Maghsoudi, K., Momen, G., Jafari, R. and Farzaneh, M., 2018. Direct replication of micro-nanostructures in the fabrication of superhydrophobic silicone rubber surfaces by compression molding. Appl. Surf. Sci. 458: 619-628.
Maghsoudi, K., Momen, G., Jafari, R. and Farzaneh, M., 2019. Rigorous testing to assess the self-cleaning properties of an ultra-water-repellent silicone rubber surface. Surf. Coat. Tech. 374: 557-568.
Maghsoudi, K., Vazirinasab, E., Jafari, R. and Momen, G., 2020. Evaluating the effect of processing parameters on the replication quality in the micro compression molding of silicone rubber. Materials Manufacturing Processes: 1-9.
Maghsoudi, K., Vazirinasab, E., Momen, G. and Jafari, R., 2020. Advances in the fabrication of superhydrophobic polymeric surfaces by polymer molding processes. Ind. Eng. Chem. Res.
Milionis, A., Loth, E. and Bayer, I. S., 2016. Recent advances in the mechanical durability of superhydrophobic materials. Adv. Colloid Interface Sci. 229: 57-79.

Mobarakeh, L. F., Jafari, R. and Farzaneh, M., 2018. Robust icephobic, and anticorrosive plasma polymer coating. Cold Reg. Sci. Technol. 151: 89-93.
Momen, G. and Farzaneh, M., 2014. Facile approach in the development of icephobic hierarchically textured coatings as corrosion barrier. Applied Surface Science 299: 41-46.
Momen, G., Jafari, R. and Farzaneh, M., 2015. Ice repellency behaviour of superhydrophobic surfaces: Effects of atmospheric icing conditions and surface roughness. Appl. Surf. Sci. 349: 211-218.
Papadopoulos, P., Pinchasik, B.-E., Tress, M., Vollmer, D., Kappl, M. and Butt, H.-J. J., 2018. Wetting of soft superhydrophobic micropillar arrays. Soft Matter 14(36): 7429-7434.
Qiang, M., Chen, F., Zhou, A., Xiao, S., Zhang, J. and Wang, Z., 2007. Impacts of wind velocity on sand and dust deposition during dust storm as inferred from a series of observations in the northeastern Qinghai–Tibetan Plateau, China. Powder Technol. 175(2): 82-89.
Rønneberg, S., He, J. and Zhang, Z., 2020. The need for standards in low ice adhesion surface research: a critical review. J. Adhes. Sci. Technol. 34(3): 319-347.
Ryerson, C. C., 2011. Ice protection of offshore platforms. Cold Reg. Sci. Technol. 65(1): 97-110.
Sansom, C., Comley, P., King, P., Almond, H., Atkinson, C. and Endaya, E., 2015. Predicting the effects of sand erosion on collector surfaces in CSP plants. Energy Procedia 69: 198-207.
Shen, Y., Tao, H., Chen, S., Zhu, L., Wang, T. and Tao, J., 2015. Icephobic/anti-icing potential of superhydrophobic Ti6Al4V surfaces with hierarchical textures. RSC Adv. 5(3): 1666-1672.
Stenroos, C., 2015. Properties of icephobic surfaces in different icing conditions.
van Boxel, J. H., 1997. Numerical model for the fall speed of rain drops in a rain fall simulator. Workshop on wind and water erosion.
Vazirinasab, E., Jafari, R. and Momen, G., 2018. Application of superhydrophobic coatings as a corrosion barrier: A review. Surf. Coat. Tech. 341: 40-56.
Vazirinasab, E., Jafari, R. and Momen, G., 2019. Evaluation of atmospheric-pressure plasma parameters to achieve superhydrophobic and self-cleaning HTV silicone rubber surfaces via a single-step, eco-friendly approach. Surf. Coat. Tech. 375: 100-111.
Vazirinasab, E., Maghsoudi, K., Jafari, R. and Momen, G., 2020. A comparative study of the icephobic and self-cleaning properties of Teflon materials having different surface morphologies. J. Mater. Process. Technol. 276: 116415.
Wang, Z., Yin, C., Luo, Y., Chen, L., Zhou, Y., He, C., Fang, P., Peng, X. and Huang, Z., 2018. Effect of aluminum hydroxide on low-molecular-weight siloxane distribution and microstructure of high-temperature vulcanized silicone rubber. J. Appl. Polym. Sci. 135(6): 45803.
Work, A. and Lian, Y., 2018. A critical review of the measurement of ice adhesion to solid substrates. Prog. Aerosp. Sci. 98: 1-26.
Yan, Z., Liang, X., Wu, C., Bao, W., Li, S. and Liu, Y., 2015. Aging and recovery of superhydrophobic silicone rubber under electrical and non-electrical stresses. IEEE Conference on Electrical Insulation and Dielectric Phenomena (CEIDP), IEEE.
Yancheshme, A. A., Momen, G. and Aminabadi, R. J., 2020. Mechanisms of ice formation and propagation on superhydrophobic surfaces: A review. Adv. Colloid Interface Sci.: 102155.
Yao, Y., Li, C., Zhang, H. and Yang, R., 2017. Modelling the impact, spreading and freezing of a water droplet on horizontal and inclined superhydrophobic cooled surfaces. Appl. Surf. Sci. 419: 52-62.
Yuan, D., Zhang, T., Guo, Q., Qiu, F., Yang, D. and Ou, Z., 2018. Recyclable biomass carbon@ SiO2@ MnO2 aerogel with hierarchical structures for fast and selective oil-water separation. Chem. Eng. J. 351: 622-630.
Zhang, H., Tu, Y., Lu, Y., Xu, Z., Chen, C. and Xie, L., 2012. Study on aging characteristics of silicone rubber insulator sheds using FTIR. IEEE International Symposium on Electrical Insulation, IEEE.
Zou, M., Beckford, S., Wei, R., Ellis, C., Hatton, G. and Miller, M., 2011. Effects of surface roughness and energy on ice adhesion strength. Appl. Surf. Sci. 257(8): 3786-3792.